Resonant wedge-plasmon modes in single-crystalline gold nanoplatelets

Lin Gu,[1,*] Wilfried Sigle,[1,†] Christoph T. Koch,[1] Burcu Ögüt,[1] Peter A. van Aken,[1] Nahid Talebi,[1,2] Ralf Vogelgesang,[3] Jianlin Mu,[4] Xiaogang Wen,[4] and Jian Mao[4]

[1]*Max Planck Institute for Metals Research, Heisenbergstraße 3, D-70569 Stuttgart, Germany*

[2]*Photonics Research Laboratory, Center of Excellence for Applied Electromagnetic Systems, School of Electrical and Computer Engineering, University of Tehran, North Kargar Ave., Tehran, Iran*

[3]*Max Planck Institute for Solid State Research, Heisenbergstraße 1, D-70569 Stuttgart, Germany*

[4]*School of Material Science and Engineering, Sichuan University, 610065 Chengdu, People's Republic of China*

(Received 22 December 2010; revised manuscript received 1 March 2011; published 24 May 2011)

Using energy-filtered transmission electron microscopy we measured surface-plasmon resonances of gold nanoplatelets with different shapes and edge lengths at high spatial resolution. We find equidistant maxima of the energy-loss probability along the platelet edges. The plasmon dispersion of the different geometries is very similar, i.e., hardly dependent on specimen shape. The experimental results are verified by means of finite-difference time-domain calculations which reveal the presence of wedge-plasmon polaritons propagating along the platelet edges. At platelet corners, apart from radiative losses, wedge-plasmon polaritons are partially reflected or transmitted to neighboring edges. The interference of all these contributions leads to the observed plasmon resonance modes. This is an essential step towards a thorough understanding of plasmon eigenmodes in prismatic nanoplatelets.

DOI: 10.1103/PhysRevB.83.195433 PACS number(s): 73.20.Mf, 68.37.Lp, 79.20.Uv

I. INTRODUCTION

Coherent oscillations of electrons at metal surfaces excited by external electromagnetic radiation are called surface plasmons. A condition for the occurrence of surface plasmons is that at the frequency ω of the exciting radiation the dielectric function of the material satisfies the condition $\mathrm{Im}[\varepsilon(\omega)] \ll \mathrm{Re}[-\varepsilon(\omega)]$.[1] In the case of confined surfaces, as is the case for small metal particles, surface-plasmon resonances (SPRs) may occur, the shape and resonance frequency of which are also defined by the particle geometry. Noble metal nanoparticles with sizes smaller than the wavelength of the excited radiation can support localized surface-plasmon resonances and exhibit optical properties enabling a variety of applications, including surface-enhanced Raman spectroscopy (SERS),[2,3] chemical and biological sensing,[4,5] lithographic fabrication,[6,7] plasmonic waveguides,[8] and second-harmonic generation.[9] Recent investigations in the field of plasmonics have focused on metal nanostructures substantially smaller than the wavelength of light. Consequently, the optical response reflects the properties of the local electric field at the particle and has a predominantly dipole character which can be optimized by manipulating the system geometry.[10–12] By increasing the particle size, the optical excitation of higher-order harmonics, i.e., multipolar plasmon resonances, becomes possible and significantly modifies the optical properties.[13,14] Multipolar surface-plasmon modes were demonstrated spectrally in the visible and near-infrared regions;[15,16] meanwhile, correlated theoretical approaches were developed.[17,18] In the long-wavelength regime where the surface-plasmon dispersion is close to the light line, the combined excitation consisting of a surface plasmon and an electromagnetic wave is called a surface-plasmon polariton (SPP).[19–21] SPPs have attracted considerable attention due to their potential applications in optical circuits and optical computers.

Surface-plasmon resonance phenomena have been widely studied using optical approaches such as scanning near-field optical microscopy and dark-field spectroscopy.[12,22] Measuring small energy losses of fast electrons in a transmission electron microscope (TEM) provides an alternative access to investigate local SPRs with high spatial resolution by using a focused electron beam.[23–25] The combination of scanning transmission electron microscopy (STEM) with electron-energy-loss spectroscopy (EELS) allows plasmon mapping at a spatial resolution better than $\lambda/40$. With the advent of high-performance electron monochromators and in-column energy filters, energy-filtering transmission electron microscopy (EFTEM) utilizing a broad electron beam and parallel acquisition in the low energy-loss range, has emerged as a technique that offers rapid data collection and outstanding spatial sampling.[26–28]

Here we demonstrate mapping of plasmon resonances at the surfaces of ~70-nm-thick single-crystalline gold nanoplatelets fabricated by a solution-phase microwave-mediated method using the EFTEM approach. The spatial distribution of the resonances up to fourth order was revealed on triangular, truncated-triangular, and hexagonal nanoplatelets. We found that the dispersion relationships for the different geometries are very similar and depend mainly on the length of the platelet sides. Finite-difference time-domain (FDTD) calculations show that this is due to the occurrence of wedge plasmons along the nanoparticle rim.

II. EXPERIMENT

Triangular noble metal nanoplatelets and snipped triangular nanoplatelets were prepared by either solution-phase light-mediated syntheses or thermal growth techniques.[29–33] Here we use the fabrication of Au nanoplatelets and truncated nanoplatelets by a microwave-mediated method. 0.5 ml of 0.1 M $HAuCl_4$ (chloroauric acid) aqueous solution was prepared in a teflon bottle followed by adding 0.144 g of glucose and 0.03 g of polyvinylpyrrolidone (PVP, molecular weight

≈ 30 000) to the solution. The mixture was dissolved in 15 ml of EG (ethylene glycol) solution and stirred for 5 min to form a solution yellowish in color. The solution was subsequently exposed to microwave irradiation in a household microwave oven (Galanz: G80D23CSL-Q6). The total reaction time was 10 min at an average power of 250 W. After the process, the color of the solution had noticeably changed to reddish-brown. The final product solution was then centrifuged at 13 000 rpm for 10 min before washing three times in distilled water and ethanol, consecutively.

Specimens of single-crystalline Au nanoplatelets for TEM investigation were drop coated on 30-nm-thick silicon nitride membranes. EFTEM and EELS experiments were performed using the Zeiss Sub-eV-Sub-Ångstrom-Microscope (SESAM) (Carl Zeiss, Oberkochen, Germany) equipped with an electrostatic Ω-type monochromator and an in-column MANDOLINE filter offering very high dispersion of the energy-loss spectrum. The SESAM microscope delivers outstanding stability and electron optical performance which allows valence EELS and valence EFTEM experiments with both high energy and high spatial resolution to be performed.[34–36] The energy resolution of the microscope defined by the full width at half maximum of the elastic zero-loss peak is below 90 meV for routine applications and has already been demonstrated to be smaller than 50 meV.[37] The in-column MANDOLINE filter provides high dispersion, high transmissivity, and high isochromaticity allowing the selection of very small energy-loss windows (<0.2 eV) for diffraction and imaging applications.[38] Besides a significant enhancement of the energy resolution, the main benefit of using monochromated electrons involves a sharp drop of the intensity from the zero-loss peak tail, enabling the detection of spectral features in the UV-visible–near-infrared domain without any numerical processing. A series of energy-filtered images from 0.4 to 3.0 eV energy loss (corresponding to wavelengths from 400 to 3000 nm) were acquired with a collection of semiangles of 6 mrad and an energy-selecting window of 0.2 eV; thus two-dimensional spatial distributions of SPRs in the energy range of interest can be mapped close to nm resolution. Specimen thickness was determined by EELS from the ratio of zero-loss intensity and total spectral intensity.[39]

III. THREE-DIMENSIONAL-FDTD SIMULATION

Three-dimensional finite-difference time-domain (3D-FDTD) calculations were used to verify the obtained experimental data. The codes were developed at the Photonics Research Laboratory, Tehran.[40,41] For these calculations the simulation domain was discretized with cubic cells having an edge length of 5 nm. The second-order absorbing boundary condition was exploited to terminate the simulation domain. Moreover, additive sources in the form of either harmonic plane waves or focused wideband Ricker wavelets[42] were used to obtain the modal field profiles or resonance spectra, respectively. The maximum number of time steps in our simulation was 2×10^4. In order to compute the resonance spectra, the integral intensity of the electric field over the samples was computed. For the Au permittivity we used a Drude model extended by two critical-point functions[43] in order to account for intra- and interband transitions. This model is in close agreement with experimental data.

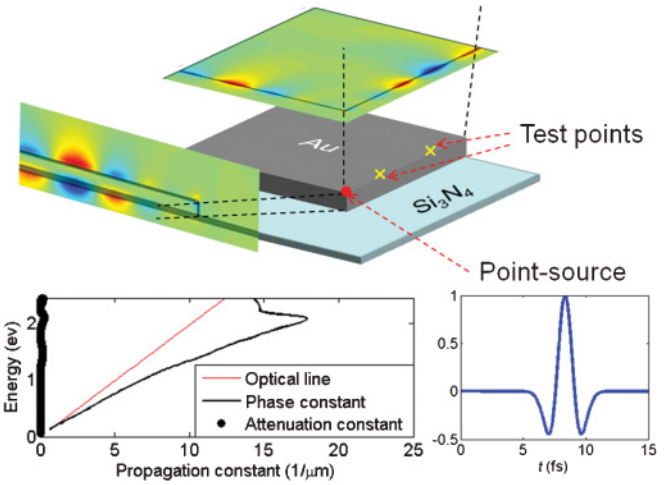

FIG. 1. (Color online) Scheme for computing the propagation constant of wedge-plasmon modes using 3D-FDTD. A wideband localized point source in the form of a Ricker wavelet (bottom right) was implemented at the red dot. The temporal evolution of the field components was detected at positions marked by yellow crosses.

In order to compute the propagation constant of the wedge-plasmon mode, we have considered a semi-infinite gold edge with an opening angle of 90°, as shown in Fig. 1. An additive source point was introduced in the form of a Ricker-wavelet temporal function at the position depicted in Fig. 1. This source gives rise to two plasmonic waves propagating along the wedges. The electromagnetic field components are computed at two introduced test points with the locations depicted in

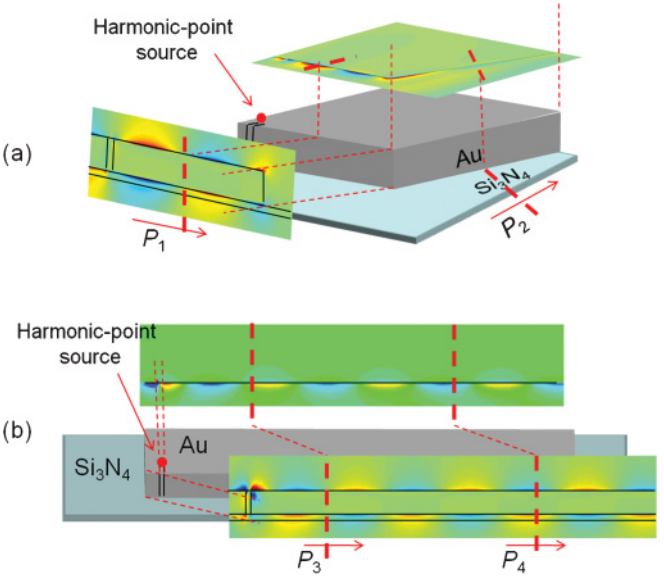

FIG. 2. (Color online) (a) Scheme for computing the transmission and reflection coefficients of the wedge-plasmon mode around a bend using 3D-FDTD. A harmonic wideband point source was introduced at the position of the red dot. Power propagation was monitored at planes indicated by red lines. This was used to calculate reflected and transmitted power. (b) Scheme for calibration of the data obtained in (a).

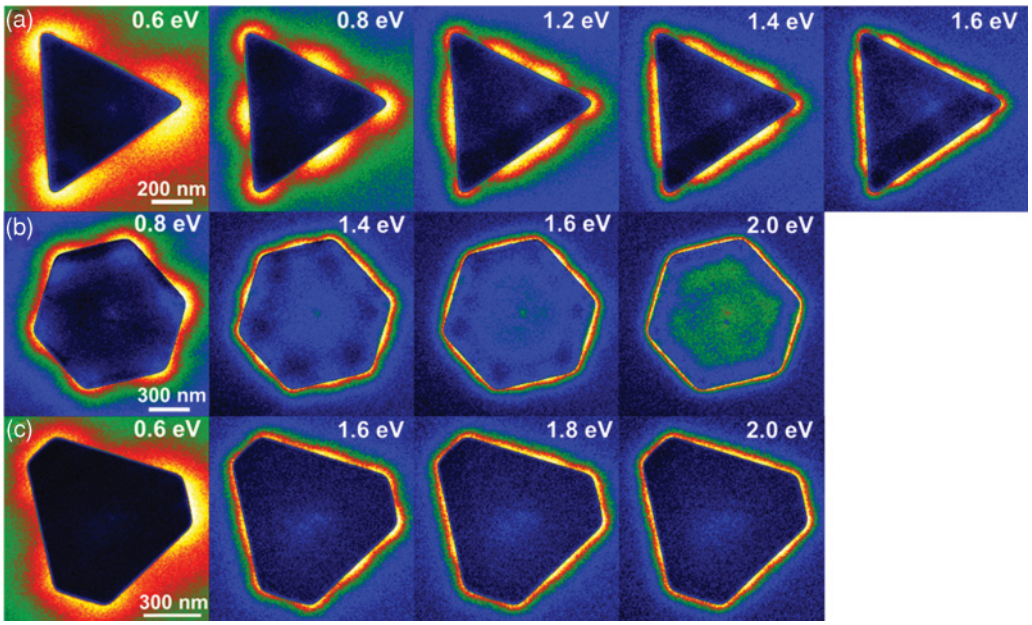

FIG. 3. (Color online) Energy-filtered images of the (a) triangular, (b) hexagonal, and (c) truncated triangular Au nanoplatelets. Colors indicate energy-loss probabilities using a temperature color scale. Low probability is indicated as blue (dark) and maximum probability as yellow (bright). The energy loss is displayed for each figure.

Fig. 1, over the whole simulation time. Then the discrete Fourier transforms of the field components are computed. Each electromagnetic field component computed at the two test points should satisfy the following equation:

$$\varphi(\vec{p}_2) = \exp(\gamma\,|\vec{p}_2 - \vec{p}_1|)\,\varphi(\vec{p}_1), \tag{1}$$

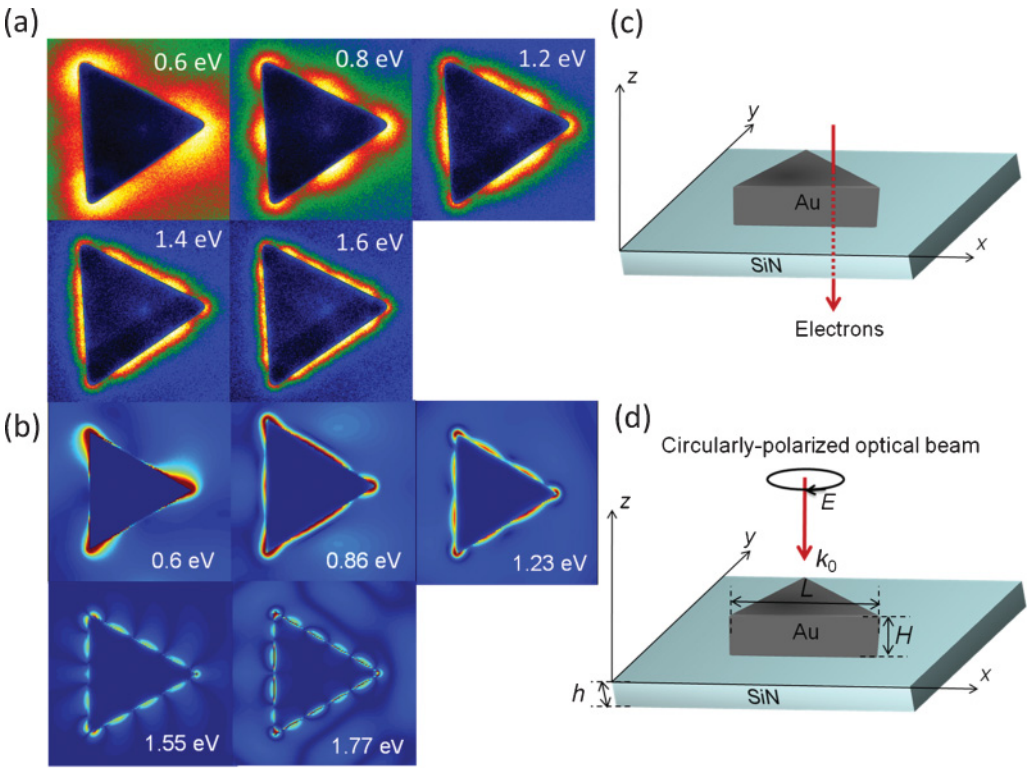

FIG. 4. (Color online) Comparison between (a) experimental and (b) simulated mode profiles of the plasmonic resonances of the triangular gold nanoplatelet on a thin Si_3N_4 substrate with the dimensions $H = 70$ nm, $h = 20$ nm, and $L = 950$ nm, as a function of the energy marked on each frame. The color scale for the experimental and simulated data was normalized to the maximum intensity. The right insets show the different schemes used to excite the plasmonic modes in EELS and FDTD simulations. Circularly polarized light is used to replicate the EELS data (see text).

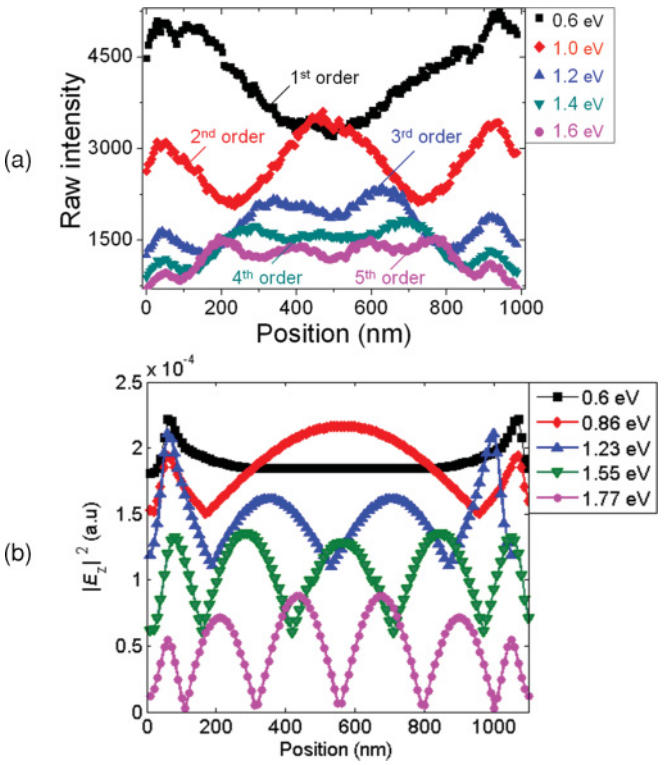

FIG. 5. (Color online) Comparison between measured and computed mode profiles along one edge of the triangular gold nanoplatelets. The data show good qualitative agreement. For quantitative agreement, rigorous calculation of the electron energy-loss process would be necessary.

where $\varphi(\vec{p}_i)$ is an arbitrary electric- or magnetic-field component at the observation point defined by $\vec{p}_i$, and γ is the complex propagation constant of the wedge-plasmon mode. Using Eq. (1), one can define a search function for computing γ:

$$F(\gamma) = \left| \frac{\varphi(\vec{p}_2)}{\varphi(\vec{p}_1)} - \exp(\gamma\,|\vec{p}_2 - \vec{p}_1|) \right|. \qquad (2)$$

The phase and attenuation constants of the wedge-plasmon mode are found by searching for the zeros of $F(\gamma)$ in the complex γ plane.

A similar approach has been used for computing the transmission (T) and reflection (R) coefficients of Table I. As shown in Fig. 2, two wedges meeting at an arbitrary angle have been considered. To excite the wedge-plasmon mode, an indentation was introduced, and a harmonic point source was located just upon the indentation. In order to calculate transmitted (P_2) and reflected (P_1) powers two planes were defined cutting the edges at positions marked by dashed lines in Fig. 2(a). These planes are normal to the wave vector of the wedge-plasmon mode. In order to distinguish between the reflected and incident power, a calibration technique is used as shown in Fig. 2(b). For this, a semi-infinite plane is considered with the same indentation and harmonic source as in Fig. 2(a). Then the power passing through the positions P_3 and P_4 [Fig. 2(b)] is computed. Using the computed powers, the T and R coefficients are computed as $T = P_2/P_4$ and $R = 1 - P_1/P_3$ at each energy.

IV. RESULTS AND DISCUSSION

The thickness of the three nanoplatelets was determined as (70 ± 15) nm, which was constant throughout the structures. This implies that coupling between the two horizontal surfaces through the bulk is negligibly small since the typical skin depth for Au is about 20–25 nm in the energy range studied here. The particles are single crystalline, which is of importance for achieving large surface-plasmon propagation lengths.[44] Energy-filtered images of the nanoplatelets are shown in Figs. 3(a)–3(c). The intensities are color coded for better visibility, and are proportional to the z-projected local photonic density of states.[45] The experimental geometry is shown in Fig. 4(c). For all particles multiple-order plasmon resonances are clearly discernible. For the case of the triangular platelet shown in Fig. 3(a), the intensity along the upper right edge is plotted in Fig. 5(a) at energy losses (wavelengths) of 0.6 (2.07 μm), 1.0 (1.24 μm), 1.2 (1.04 μm), 1.4 (0.89 μm), and

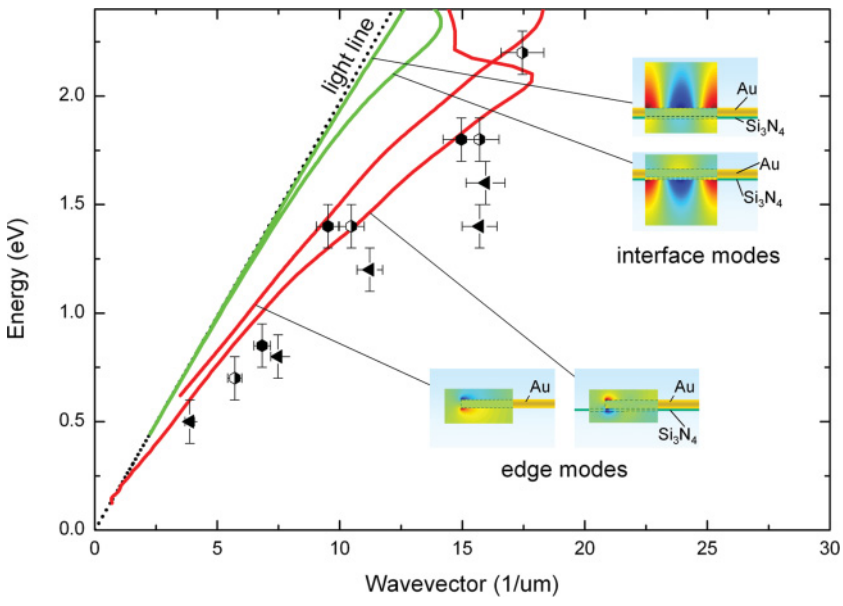

FIG. 6. (Color online) Comparison between the computed propagation constant of various plasmonic modes possible for a semi-infinite Au platelet on a Si_3N_4 substrate, and the measured wave vector of the plasmonic modes obtained from the EFTEM data (triangular symbols for the triangle and hexagonal symbols for the truncated triangle and the hexagon). The insets show the spatial distribution for the z component of the electric field.

TABLE I. Power transmission (T) and reflection (R) coefficients at platelet corners making a 60° and 120° angle, respectively. The numbers were obtained by FDTD at different energies (see Fig. 2 and text).

Energy	0.6 eV		1 eV		1.2 eV		1.4 eV		1.6 eV	
Angle	T	R	T	R	T	R	T	R	T	R
60°	0.091	0.086	0.137	0.077	0.336	0.038	0.418	0.026	0.296	0.079
120°	0.461	0.003	0.483	0.002	0.498	0.001	0.538	0.003	0.234	0.003

1.6 eV (0.78 μm). Equidistant local field enhancements are visible up to the fifth order. Similar intensity variations were found for the other nanoplatelets.

In order to identify the origin of the observed plasmon modes we compare experimental and calculated dispersion curves. We interpret the separation of the equidistant field maxima as half a wavelength of the propagating plasmon. The measured plasmon dispersions are shown in Fig. 6. Because of the very similar dispersion, hexagonal symbols were used for both the truncated triangle and the hexagon. Triangular symbols are used for the triangle. Calculated dispersion curves are shown for the Au nanoplatelet with and without the thin Si_3N_4 membrane. We can distinguish two categories of dispersion curves. For the case of an infinitely extended Au film on a thin Si_3N_4 substrate there is a plasmon located at the interface (lower green line) and another one with field maxima on the Au surface (upper green line). Both are far from the experimental data. Secondly, dispersions of plasmon modes running along the wedges of the nanoparticles (red lines) are shown, both for a freestanding Au film and a Au film on a thin Si_3N_4 substrate. These latter two dispersion curves are close to each other, which means that the thin Si_3N_4 substrate has only little influence on these modes. Most importantly, they are much closer to the experimental data than the pure interface and surface plasmons. The remaining discrepancies can possibly be explained by subtle differences between the real wedge shape and the one used in the simulation. These results are strong evidence that it is these wedge-plasmon modes that we observe in our experiments. From the inset in Fig. 6 one can clearly see that the field maxima of the wedge plasmons are located at the upper and lower wedges.[46,47] This is not unexpected since it is well known that structural discontinuities are always connected with local field enhancement.

In order to calculate the field distributions of the plasmon eigenmodes along the wedges, a circularly polarized excitation was used in the FDTD calculations and response fields at different z positions were incoherently summed up. Since the electric-field distribution around the fast electron is azimuthally isotropic the excitation by a circularly polarized electromagnetic wave resembles the EFTEM experiment much better than the excitation by a linearly polarized wave. The situation of the EFTEM experiment can then be modeled by incoherently integrating the response of the system for one full rotation of the wave's polarization. Both EFTEM and FDTD probe the same set of eigenmodes, i.e., we expect qualitatively the same results, though not quantitatively. This is confirmed by the spatial field distributions [Fig. 4(b)] and the mode profiles along the edge of the triangle [Fig. 5(b)], which both show a remarkable resemblance to the experimental data [Figs. 4(a) and 5(a)].

An important advantage of FDTD is that the dynamics of plasmon propagation can be analyzed. This gives us further important insight into the nature of the resonant plasmonic wedge modes. For this purpose, calculations with wideband local excitations in the form of Ricker-wavelet point sources were performed for the case of the triangular platelet. The locations of the point sources have been chosen in such a way as to distinguish between symmetric and antisymmetric modes, as depicted in the inset of Fig. 7(a). In Figs. 7(b) and 7(c)

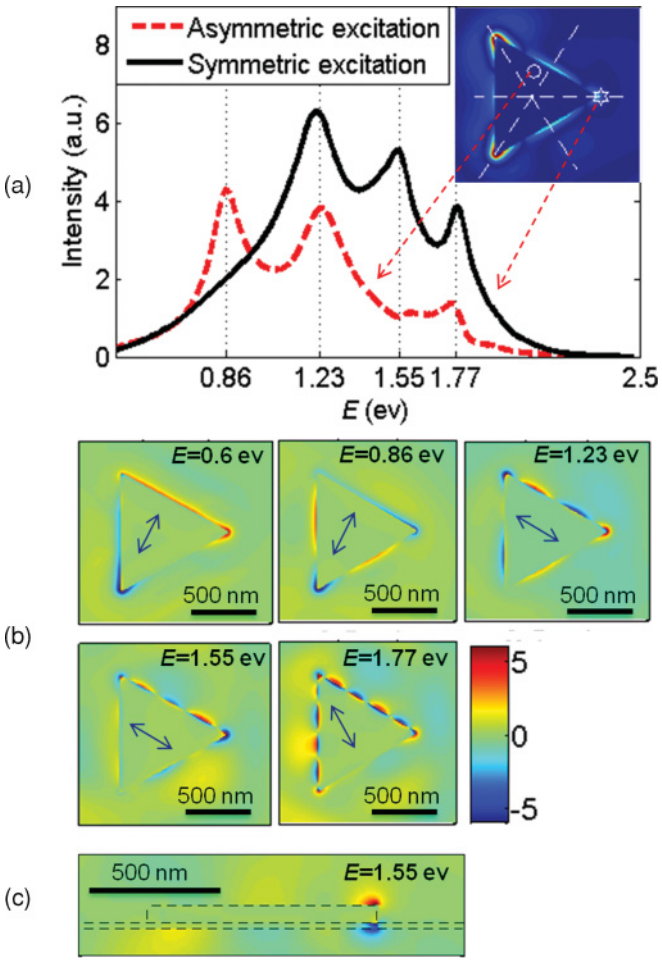

FIG. 7. (Color online) (a) Eigenmodes of the gold triangular nanoplatelets with the geometrical parameters depicted in Fig. 2, computed using FDTD with introduced wideband, localized, symmetric, and asymmetric excitations. Mode profiles at an arbitrary time, computed using FDTD for (b) top view and (c) side view.

the field distribution is shown for each resonance energy at an arbitrary time, for both top and side cross sections. In order to gain further insight into the propagation of the wedge-plasmon modes we performed FDTD calculations with local excitations at various wavelengths for the case of the triangular platelet. In Fig. 7 the field distribution is shown at each wavelength (energy). It is obvious that the wedge plasmons propagate ("transmit") around the corner of the triangle. In the case of complete transmission this effect would lead to whispering gallery modes, if the condition $\sum_{i,j}\left(\gamma L_i + \varphi_{\mathrm{tr},j}\right) = n2\pi$ is met, where γ is the propagation constant, L_i are the edge lengths of the platelet, and $\phi_{\mathrm{tr},}j$ is the phase change when the polariton propagates across the edge. In the case of complete reflection, Fabry-Pérot modes[21] are excited if $2\gamma L + \gamma_{\mathrm{left}} + \gamma_{\mathrm{right}} = n2\pi$, where L is the edge length and φ_{right} and φ_{left} are the phase changes upon reflection at the two boundaries of the edge. However, our calculations show that transmission and reflection coefficients are less than unity (Table I), i.e., we neither have the situation of a whispering gallery mode nor of a Fabry-Pérot resonator. Furthermore, we found that the sum of reflected and transmitted intensities is not equal to the excited intensity, which means that there are radiative losses at the corners. Such radiative losses at pointlike discontinuities are well known. The fractions of transmitted and reflected intensities depend on plasmon energy, as is shown in Table I. The main conclusion of these FDTD calculations is that the observed resonant behavior of the nanoplatelets originates from the interference of excited, reflected, and transmitted wedge SPPs. The relative importance of the individual contributions will depend on the size, thickness (because of coupling effects), and shape of the nanoplatelet as well as on the resonance energy.

Our interpretation of the plasmonic response of nanoplatelets became possible by the study of large nanoplatelets exhibiting multiple field maxima along their edges. In earlier studies SPRs were shown in triangular nanoplatelets[24,48] which had a circumference smaller than the resonance wavelength. Only a single field maximum along the edge was found in these studies. These SPRs are quasistatic eigenmodes of the triangles. In the present study, and also in Ref. 26, larger nanoplatelets were studied which allow us to detect modes with more than one maximum. Our simulations verify that this phenomenon is due to the *propagating* nature of SPPs along the nanoplatelet wedges. This reveals a transition from an SPR- to SPP-dominated regime when the particle circumference becomes comparable to the resonance wavelength.

Finally, we should mention that surface plasmons are also excited on the top and bottom surfaces of the nanoplatelets. However, these are much weaker than the wedge plasmons. The analysis of these modes will be addressed in an upcoming paper.

V. CONCLUSIONS

In conclusion, we showed that surface-plasmon resonances of single-crystalline gold nanoplatelets exhibit very similar behavior, only weakly depending on particle shape. Using FDTD we analyzed all plasmonic modes occurring in nanoplatelets. We found that the plasmonic behavior is dominated by wedge-plasmon modes propagating along the nanoplatelet edges, giving a very close correspondence between theory and experiment. Our results show the intriguing interplay of excited, whispering-gallery-like, and reflected SPPs in nanoplatelets.

ACKNOWLEDGMENTS

We acknowledge financial support from the European Union under the Framework 6 program under a contract for an Integrated Infrastructure Initiative, Reference 026019 (ESTEEM). X.W. thanks the National Natural Science Foundation of China (Grant No. 50872084) for supporting this research. N.T. thanks the Iran Telecommunication Research Center for financial support.

*Present address: Beijing Laboratory for Electron Microscopy, Institute of Physics, Chinese Academy of Sciences, China.
†Corresponding author: sigle@mf.mpg.de

[1] F. J. García de Abajo, Rev. Mod. Phys. **79**, 1267 (2007).
[2] M. Moskovits, Rev. Mod. Phys. **57**, 783 (1985).
[3] S. Kühn, U. Håkanson, L. Rogobete, and V. Sandoghdar, Phys. Rev. Lett. **97**, 017402 (2006).
[4] A. J. Haes, L. Chang, W. L. Klein, and R. P. Van Duyne, J. Am. Chem. Soc. **127**, 2264 (2005).
[5] G. Raschke, S. Kowarik, T. Franzl, C. Sönnichsen, T. A. Klar, and J. Feldmann, Nano Lett. **3**, 935 (2003).
[6] W. Srituravanich, N. Fang, C. Sun, Q. Luo, and X. Zhang, Nano Lett. **4**, 1085 (2004).
[7] A. Sundaramurthy, J. P. Schuck, N. R. Conley, D. P. Fromm, G. S. Kino, and W. E. Moerner, Nano Lett. **6**, 355 (2006).
[8] S. A. Maier, P. G. Kik, and H. A. Atwater, Appl. Phys. Lett. **81**, 1714 (2002).
[9] C. K. Chen, A. R. B. de Castro, and Y. R. Shen, Phys. Rev. Lett. **46**, 145 (1981).
[10] M. Rang, A. C. Jones, F. Zhou, Z.-Y. Li, B. J. Wiley, Y. Xia, and M. B. Raschke, Nano Lett. **8**, 3357 (2008).
[11] L. J. Sherry, R. Jin, R. C. A. Mirkin, G. C. Schatz, and Van R. P. Duyne, Nano Lett. **6**, 2060 (2006).
[12] J. J. Mock, M. Barbic, D. R. Smith, D. A. Schultz, and S. Schultz, J. Chem. Phys. **116**, 6755 (2002).
[13] N. Félidj, J. Grand, G. Laurent, J. Aubard, G. Lévi, A. Hohenau, N. Galler, F. R. Aussenegg, and J. R. Krenn, J. Chem. Phys. **128**, 094702 (2008).
[14] J. R. Krenn, G. Schider, W. Rechberger, B. Lamprecht, A. Leitner, and F. R. Aussenegg, Appl. Phys. Lett. **77**, 3379 (2000).
[15] A. S. Kumbhar, M. K. Kinnan, and G. Chumanov, J. Am. Chem. Soc. **127**, 12444 (2005).
[16] J. E. Millstone, S. Park, K. L. Shuford, L. Qin, G. C. Schatz, and C. A. Mirkin, J. Am. Chem. Soc. **127**, 5312 (2005).
[17] K. L. Shuford, M. A. Ratner, and G. C. Schatz, J. Chem. Phys. **123**, 114713 (2005).
[18] E. Hao and G. C. Schatz, J. Chem. Phys. **120**, 357 (2004).
[19] A. V. Zayats and I. I. Smolyaninov, J. Opt. A: Pure Appl. Opt. **5**, S16 (2003).
[20] N. Yamamoto and T. Suzuki, Appl. Phys. Lett. **93**, 093114 (2008).
[21] J. Dorfmüller, R. Vogelgesang, T. Weitz, C. Rockstuhl, C. Etrich, T. Pertsch, F. Lederer, and K. Kern, Nano Lett. **9**, 2372 (2009).

[22] J. R. Krenn, A. Dereux, J. C. Weeber, E. Bourillot, Y. Lacroute, J. P. Goudonnet, G. Schider, W. Gotschy, A. Leitner, F. R. Aussenegg, and C. Girard, Phys. Rev. Lett. **82**, 2590 (1999).
[23] M. Chu, V. Myroshnychenko, C. Chen, J. Deng, C. Mou, and F. J. García de Abajo, Nano Lett. **9**, 399 (2009).
[24] J. Nelayah, M. Kociak, O. Stéphan, F. J. García de Abajo, M. Tencé, L. Henrard, D. Taverna, I. Pastoriza-Santos, L. M. Liz-Marzán, and C. Colliex, Nat. Phys. **3**, 348 (2007).
[25] M. Bosman, V. J. Keast, M. Watanabe, A. I. Maaroof, and M. B. Cortie, Nanotechnology **18**, 165505 (2007).
[26] J. Nelayah, L. Gu, W. Sigle, C. T. Koch, I. Pastoriza-Santos, Liz-Marzán, and P. A. van Aken, Opt. Lett. **34**, 1003 (2009).
[27] W. Sigle, J. Nelayah, C. T. Koch, and P. A. van Aken, Opt. Lett. **34**, 2150 (2009).
[28] B. Schaffer, U. Hohenester, A. Trügler, and F. Hofer, Phys. Rev. B **79**, 041401 (2009).
[29] C. Xue and C. A. Mirkin, Angew. Chem., Int. Ed. **46**, 2036 (2007).
[30] R. Jin, Y. Cao, C. A. Mirkin, K. L. Kelly, G. C. Schatz, and J. G. Zheng, Science **294**, 1901 (2001).
[31] S. S. Shankar, A. Rai, B. Ankamwar, A. Singh, A. Ahmad, and M. Sastry, Nat. Mater. **3**, 482 (2004).
[32] N. Malikova, I. Pastoriza-Santos, M. Schierhorn, N. A. Kotov, and L. M. Liz-Marzán, Langmuir **18**, 3694 (2002).
[33] J. E. Millstone, S. J. Hurst, G. S. Métraux, J. I. Cutler, and C. A. Mirkin, Small **5**, 646 (2009).
[34] H. Uhlemann and H. Rose, Optik (Stuttgart) **96**, 163 (1994).
[35] H. Rose, Ultramicroscopy **78**, 13 (1999).
[36] L. Gu, V. Srot, W. Sigle, C. T. Koch, P. A. van Aken, F. Scholz, S. B. Thapa, C. Kirchner, M. Jetter, and M. Rühle, Phys. Rev. B **75**, 195214 (2007).
[37] E. Essers, G. Benner, T. Mandler, S. Meyer, D. Mittmann, M. Schnell, and R. Höschen, Ultramicroscopy **110,** 971 (2010).
[38] C. T. Koch, W. Sigle, R. Höschen, M. Rühle, E. Essers, G. Benner, and M. Matijevic, Microsc. Microanal. **12**, 506 (2006).
[39] R. F. Egerton, *Electron Energy-Loss Spectroscopy in the Electron Microscope*, 2nd ed. (Plenum Press, New York, 1996).
[40] N. Talebi and M. Shahabadi, J. Opt. Soc. Am. B **27**, 2273 (2010).
[41] N. Talebi and M. Shahabadi, J. Phys. D **43**, 135302 (2010).
[42] N. V. Kartantzis and T. D. Tsiboukis, *Higher-Order FDTD Schemes for Waveguide and Antenna Structures* (Morgan & Claypool, San Rafael, CA, 2006), p. 108.
[43] P. A. Tirkas, C. A. Balanis, and R. A. Renaut, IEEE Trans. Antennas Propag. **40**, 1215 (1992).
[44] H. Ditlbacher, A. Hohenau, D. Wagner, U. Kreibig, M. Rogers, F. Hofer, F. R. Aussenegg, and J. R. Krenn, Phys. Rev. Lett. **95**, 257403 (2005).
[45] F. J. García de Abajo and M. Kociak, Phys. Rev. Lett. **100**, 106804 (2008).
[46] J. G. Van Bladel, *Electromagnetic Fields*, edited by D. G. Dudley (Wiley, Hoboken, NJ, 2007).
[47] J. Aizpurua, A. Howie, and F. J. Garcia de Abajo, Phys. Rev. B **60**, 11149 (1999).
[48] J. Nelayah, M. Kociak, O. Stéphan, N. Geuquet, L. Henrard, F. J. García de Abajo, I. Pastoriza-Santos, L. M. Liz-Marzan, and C. Colliex, Nano Lett. **10**, 902 (2010).